



Event-based contact angle measurements inside porous media using time-resolved micro-computed tomography

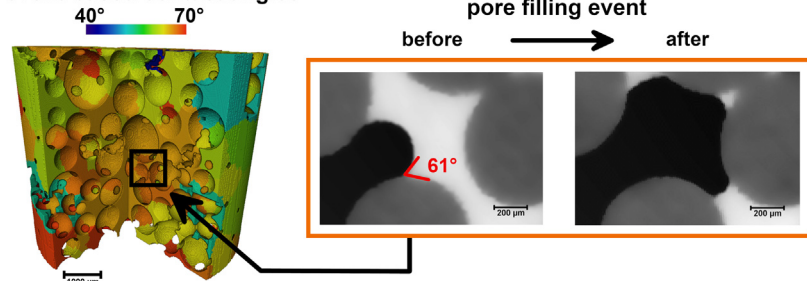
Arjen Mascini^{a,*}, Veerle Cnudde^{a,b}, Tom Bultreys^a

^a PProGress/UGCT, Dept. of Geology, Ghent University, Krijgslaan 281/ S8, 9000 Ghent, Belgium

^b Environmental Hydrogeology, Dept. of Earth Sciences, Utrecht University, Princetonlaan 8a, 3584 Utrecht, the Netherlands

GRAPHICAL ABSTRACT

event-based contact angles



ARTICLE INFO

Article history:

Received 28 January 2020

Revised 25 March 2020

Accepted 26 March 2020

Available online 27 March 2020

Keywords:

Contact angle
Pore-scale
Wettability
Multiphase flow
Porous media
Imaging
X-ray micro-tomography
Interfacial curvature
Haines jump
Primary drainage

ABSTRACT

Hypothesis: Capillary-dominated multiphase flow in porous materials is strongly affected by the pore walls' wettability. Recent micro-computed tomography (mCT) studies found unexpectedly wide contact angle distributions measured on static fluid distributions inside the pores. We hypothesize that analysis on time-resolved mCT data of fluid invasion events may be more directly relevant to the fluid dynamics.

Experiment: We approximated receding contact angles locally in time and space on time-resolved mCT datasets of drainage in a glass bead pack and a limestone. Whenever a meniscus suddenly entered one or more pores, geometric and thermodynamically consistent contact angles in the surrounding pores were measured in the time step just prior to the displacement event. We introduced a new force-based contact angle, defined to recover the measured capillary pressure in the invaded pore throat prior to interface movement.

Findings: Unlike the classical method, the new geometric and force-based contact angles followed plausible, narrower distributions and were mutually consistent. We were unable to obtain credible results with the thermodynamically consistent method, likely because of sensitivity to common imaging artifacts and neglecting dissipation. Time-resolved mCT analysis can yield a more appropriate wettability characterization for pore scale models, despite the need to further reduce image analysis uncertainties.

© 2020 The Authors. Published by Elsevier Inc. This is an open access article under the CC BY license (<http://creativecommons.org/licenses/by/4.0/>).

1. Introduction

Multiphase flow in porous materials is crucial for e.g. safe sub-surface CO₂ storage [1], groundwater remediation [2] and efficient

PEM fuel cells [3,4]. This process is strongly affected by the porous medium's wettability: its affinity to be in contact with one fluid over another [5]. The wettability, typically expressed as a contact angle between the solid and the fluids, induces capillary forces which exert a strong influence on fluid displacement [6]. Drainage is the displacement of a wetting fluid by a non-wetting fluid, while the reverse process is called imbibition [7]. Fundamentally,

* Corresponding author.

E-mail address: Arjen.Mascini@UGent.be (A. Mascini).

wettability is a function of the intermolecular forces between the fluids and the solid surface (including any coatings or impurities on it). In addition, most natural materials contain surface roughness from the nanometer scale upwards, which influences the effective contact angle observed at larger scales [8]. Due to local variations in mineralogy, surface roughness and coating, contact angles in porous media are often hysteretic, scale-dependent and variable throughout the pore space [5,9–18]. One of the main open standing questions is therefore how to define and measure local wettability characteristics throughout the pore space with relevance to multiphase fluid dynamics. This is particularly important to inform pore-scale computational models [19–21].

Recent work has shown that contact angles can be measured by geometrical analysis on a 3D image of fluids in the pore space where the interfaces between the fluids remain static. Such images are typically acquired using micro-computed X-ray tomography (mCT), which has been established as an important tool to investigate multiphase flow at the pore scale in recent years [7,22–25]. Local measurements of geometrical contact angles in the pore space can be made based on visual observation [22,26], automated algorithms [27,28] or methods based on the deficit curvature of the solid and fluid interfaces [29]. However, these measurements were shown to result in unexpectedly wide distributions of contact angles which are difficult to interpret and to use in pore scale models [30,31]. This is not fully explained by the significant uncertainty on determining the three-phase contact line and the normal to the rough solid surface, caused by partial volume effects and other imaging artefacts common in mCT [32].

None of the methods discussed so far take into account that contact angles measured on static fluid distributions may not be directly relevant to dynamic fluid displacements during drainage and imbibition. Due to unresolved roughness on the solid surface, contact angles can be hysteretic: at a pinned contact line in any pore, the contact angle can vary between an advancing and a receding value, at which the contact line finally starts to move. Furthermore, the location of the contact line in combination with the pore shape at the time of observation, as well as the equilibration time before imaging, likely also influence the observed contact angles [33,34]. Such effects cannot be discerned from an image of a fluid distribution at one specific time. Blunt et al. [31] addressed these concerns by indirectly estimating a thermodynamically consistent contact angle based on energy conservation. They compared mCT images of fluids in a rock sample at the start and end of imbibition, and then equated the pressure-volume work, estimated by measuring the curvature of the fluid-fluid interface and the saturation change, to the interfacial energy stored in the system. The latter can be expressed in function of interfacial areas and a “thermodynamically consistent” contact angle. The sensitivity to contact line and solid surface normal estimation is therefore reduced or eliminated. Furthermore, this definition aims to take the effects of unresolved solid surface features into account, as it should yield an effective value related to the fluid displacement. Yet, two important issues remain. First, the method assumes that the invasion process can be approximated as being reversible, while this is unlikely to hold for general displacements. Seth and Morrow [35] found that up to 84% of the pressure-volume work during drainage of a limestone was dissipated. Second, the method provides a single contact angle value for the whole sample, rather than a localized measurement.

In this work, we propose to estimate pore-scale (receding) contact angles that are relevant to fluid displacement by analyzing time-resolved mCT datasets. First, we identified the time and location of pores in which fluid displacements took place during drainage. Then, geometric and thermodynamically consistent contact angles were computed on a pore-by-pore basis for each single displacement event at the time just before displacement. We

introduce a new force-based receding contact angle definition derived from the measured curvature of a fluid meniscus which triggers it to move through a pore throat (i.e. a Haines jump). The method was tested on two publicly available drainage datasets [36,37].

The methodology and the experimental data are described in Section 2. In Section 3.1, the results from the detection of pore filling events are discussed, followed by a validation of the interfacial curvature analysis by experimental capillary pressure data in Section 3.2. In Section 3.3, the novel time-resolved contact angle measurements are compared to the prior static approach and to each other. This is followed by conclusions and discussion of the current limitations of the method in Section 4.

2. Materials and methods

In the following section, the conceptual framework for this study is first introduced, followed by a brief overview of the experimental data and a detailed description of the image analysis workflow used to identify filling events and calculate force-based, geometric and thermodynamically consistent contact angles.

2.1. Contact angles and displacement events

At low capillary numbers, drainage takes place as a sequence of unstable fluid redistribution events (Haines jumps) every few (tens of) seconds, interspersed by smooth reversible displacement [38–41]. During the smooth reversible displacement, the contact line can remain (nearly) static close to a local constriction (‘pore throat’) while the curvature of the interface increases due to the increasing capillary pressure (Fig. 1), as described by the Young-Laplace equation:

$$P_c = \sigma \left(\frac{1}{R_1} + \frac{1}{R_2} \right) = 2\kappa\sigma \quad (1)$$

where σ is the interfacial tension, R_1 and R_2 are the principle radii of curvature of the fluid-fluid interface and κ is its mean curvature.

When the pressure difference between the two fluids exceeds a certain capillary pressure threshold, an irreversible displacement takes place and the interface abruptly enters one or more neighboring pores (local dilations in the pore space). This threshold is determined by the geometry of the pore throat through which the interface has to pass – the narrower the throat, the higher the threshold – as well as by the local wettability. For example, the associated threshold curvature κ_{thr} in a cylindrical pore throat is given by the well-known Young-Laplace pressure:

$$P_{c,thr} = 2\sigma\kappa_{thr} = \frac{2\sigma\cos(\theta)}{r} \quad (2)$$

where θ is the receding contact angle measured through the densest phase, and r is the throat radius. Therefore, the local wettability in a pore throat can be characterized by defining a force-based receding contact angle θ_f relevant to the displacement:

$$\theta_f \equiv \arccos(\kappa_{thr}r) \quad (3)$$

Note that the force-based contact angle only yields the same value as the receding contact angle for perfectly cylindrical pore throats. However, the advantage is that it provides a direct link to the threshold capillary pressure without the need for measurements at or near the rough solid surface, which are highly dependent on the image resolution and the scale of surface roughness features. Furthermore, Eq. (3) can in principle be extended to arbitrarily complex geometrical pore throat models, e.g. pore throats with triangular [42] or hyperbolic polygonal cross-sections [43]. In this paper, we used the cylindrical model to obtain a first order

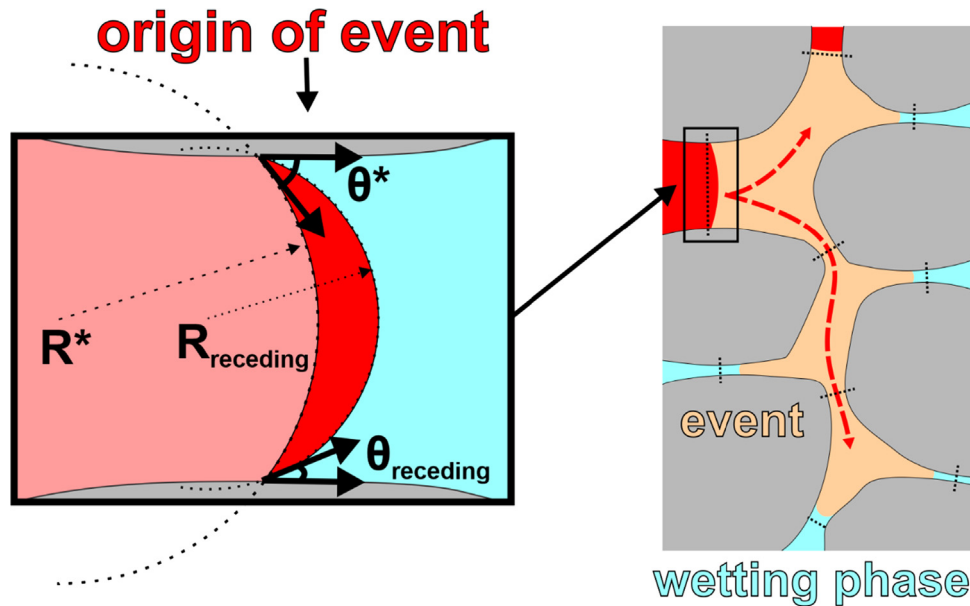


Fig. 1. A schematic drawing of a Haines jump during primary drainage. **Left box:** at time T-1 the main terminal meniscus of the non-wetting phase (in pink) is located in a pore throat with an interface with a certain radius of curvature (R^*) and associated contact angle θ^* . Just before displacement (in red), the interface reaches a radius of curvature (R_{receding}) and an associated contact angle θ_{receding} (measured through the wetting phase and hence receding) upon which it will start to move into the next pore. R_{receding} determines the threshold capillary pressure for the event. **Right box:** in the following displacement event, three neighboring pores (indicated in orange and separated by constrictions indicated as black dotted lines) are filled by the Haines jump. Fluid distributions at T-1 are in red and at time T in orange. (For interpretation of the references to colour in this figure legend, the reader is referred to the web version of this article.)

estimate of the force-based receding contact angle for several hundreds of Haines jumps in a bead pack and a limestone. The following sections describe how θ_f can be estimated for each individual displacement event in time-resolved mCT datasets, as well as how geometrical and thermodynamically consistent contact angles were determined for comparison.

2.2. Experimental data

The proposed method places restrictions on the type of image data suitable for analysis. The flowrate used in the experiments needs to be sufficiently slow to be dominated by capillary forces (i.e. a capillary number of less than 10^{-5}). The temporal resolution needs to be fast enough to capture individual filling events and the spatial resolution needs to be sufficient to clearly resolve interfaces. In addition, pressure measurements made with an external pressure transmitter are useful to validate the obtained results. Based on this, two well-documented and publicly available primary drainage data sets were selected for analysis: one measured by Schlüter et al. on a sintered glass bead pack [36] and one mea-

sured by Singh et al. on a Ketton limestone [37]. Both experiments are unsteady-state drainage experiments in which a non-wetting phase is injected into a cylindrical sample at a low capillary number to ensure capillary dominated flow. A summary of the experimental parameters is given in Table 1. The time resolved mCT experiments resulted in a series of segmented 3D images, each representing the fluid distribution in the pore space during a discrete, short time interval in the drainage. In our analysis, we use the segmented data by [36] and [37]. The former used a modified form of Markov random field (MRF) segmentation for this, the latter a seeded watershed algorithm.

2.3. Image analysis

2.3.1. Identifying fluid filling events in time-resolved mCT datasets

As a first step in the analysis, the pore space was divided into individual pores separated by throat surfaces using a watershed algorithm implemented in the open source algorithm “pnextract” [44] (Fig. 2C). This algorithm determines the largest inscribed spheres in each pore and in each throat. Pore and throat radii were found as the radii of these inscribed spheres. To assess the fluid

Table 1

Overview of the data sets used for the image analysis. * exact flow rates were not recorded during the drainage experiments.

	glass bead pack	Ketton limestone
Sample dimension	5.8 mm dia. × 7 mm long	3.8 mm dia. × 10 mm long
Boundary condition	constant flowrate	constant pressure + tight capillary plate
Fluids	<i>n</i> -dodecane, CsCl-brine	<i>n</i> -decane, KI-brine
Interfacial tension	36mN/m	52.33mN/m
Flow rate	50 μl/h	~1–6 μl/h*
Imposed pressure drop	N/A	50 kPa
Capillary number	$4.2 \cdot 10^{-8}$	$\sim 10^{-9}$ *
Number of time steps	38	496
Time per time step	113 s	38 s
Time span (hr:min:sec)	01:13:44	5:14:08
Reconstructed voxel size	8.4 μm	3.28 μm
Reference	Schlüter et al. [36]	Singh et al. [37]

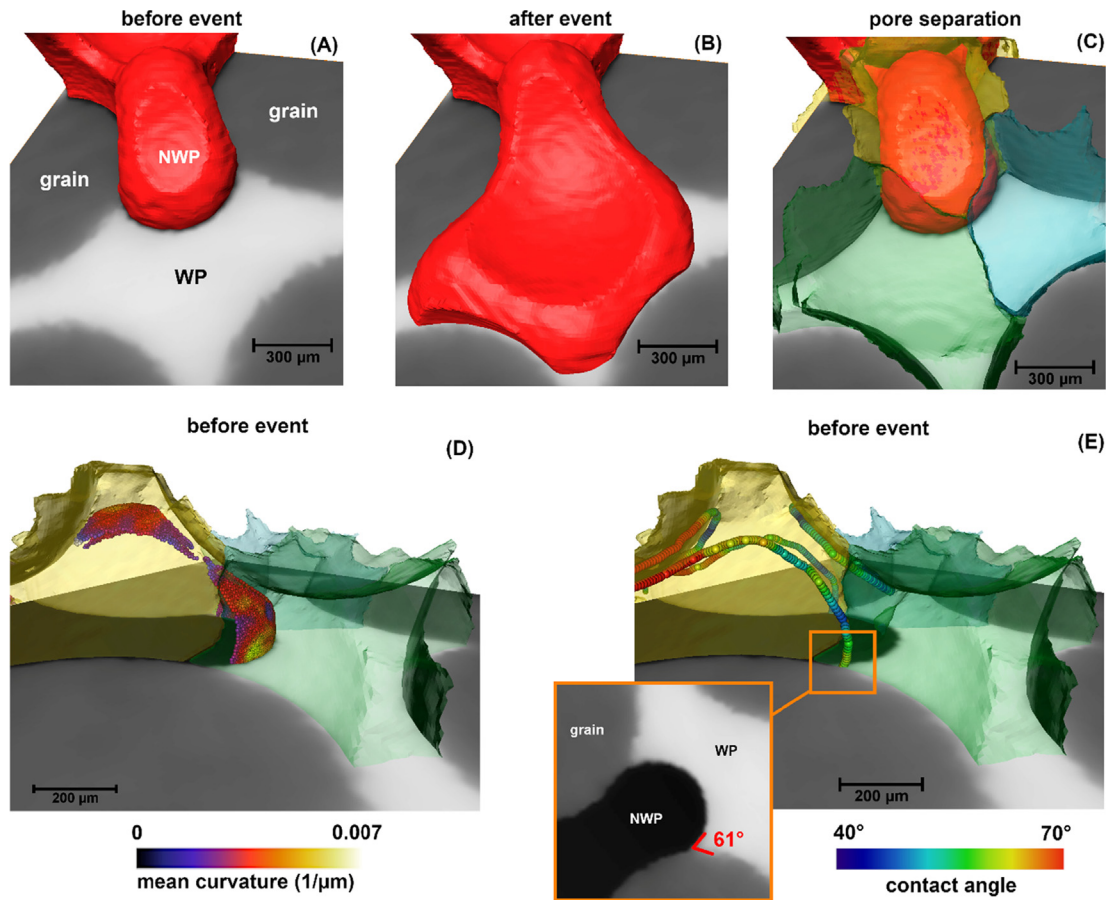


Fig. 2. Capturing and characterizing a pore filling event in the sintered glass bead pack dataset from [36]. nwp = non-wetting phase, wp = wetting phase. (A) Before the event, a NWP terminal meniscus is located at a pore throat. (B) After the event, the NWP phase moved into the neighboring pores. (C) The pore space is first subdivided into different pore bodies for analysis. Before the event, the NWP terminal meniscus interface is partially located in the yellow, blue and green pore bodies. (D) Before the event shown in (A)–(C), the interface has a mean curvature proportional to the local capillary pressure which is used to determine the force-based contact angle (rendered here from a different viewing angle than (A)–(C) for clarity). (E) the event-based geometric contact angle (62°) is calculated before the event by measuring the contact angle on the points of three-phase contact line, indicated by colored spheres. A manual measurement (small box) of the contact angle in the plane perpendicular to the grain surface is in good agreement (61°) with the event-based geometric contact angle. (For interpretation of the references to colour in this figure legend, the reader is referred to the web version of this article.)

occupancy of the center of each pore and throat, the inscribed spheres can be overlain on the drainage dataset, which is registered to a high quality dry-state image from which the PNM is extracted [44]. The occupancy is then determined by determined if the majority of the voxels in the associated inscribed sphere were filled with wetting or non-wetting phase. This was done for each pore in each time step, and “fluid filling” was consecutively found as the case where a pore changes its fluid occupancy (i.e. the fluid in the majority of its inscribed sphere’s voxels) in consecutive time steps. Connected fluid fillings in the same time step were regarded to belong to the same filling event (Fig. 1). This was done by performing a graph-based connectivity clustering of the pores filled in each time step using MATLAB. The adjacency matrix was used to cluster pores which share a connection and change fluid occupancy in the same time step into one event [45,46]. In addition, the neighboring pores are recorded for each event. Finally, the result of this analysis was a list of filling events, detailing the time of filling, the pores that were filled (including location and characterization of the pores), and the pores and throats that neighbor each filling event. The source throat of each event was found by selecting the throat neighbor with the largest throat radius.

2.3.2. Force-based receding contact angles

As defined in Section 2.1, an estimate for the force-based contact angle can be obtained by linking the local capillary pressure

which triggered the fluid redistribution to the radius of the source throat of each event. On 3D images of fluid distributions, the local capillary pressure can be estimated from the curvature of the fluid–fluid interface [45,46]. As the volume in space associated to each pore is known, it is straightforward to map point measurements of interfacial curvature to pores. At time step T-1, before a filling event, the fluid–fluid interface is located (partly) in the pores directly neighboring the event. Therefore, we determined the average fluid–fluid interfacial curvature both in pores that were invaded and in their neighbors during the time-step just before the associated filling event (Fig. 2D).

To obtain curvature values, the fluid–fluid interface was extracted from the segmented images by extracting a triangulated surface using the marching cube algorithm [47] in Avizo (ThermoFisher Scientific). Constrained surface smoothing using a Gaussian filter with an extent of 3 voxels was performed, analogous to the method described in [48]. Mean surface curvature was calculated using the eigenvalues and eigenvectors of a quadratic form fitted locally to the surface. The accuracy of this calculation is limited by the finite resolution of the images, especially in regions close to the three-phase contact line, where partial volume effects add to the uncertainty, and in arc-meniscus sections of the fluid–fluid interface [19,46,48,49]. The curvature data points were filtered based on several criteria to account for this. First, all data points with a curvature corresponding to a radius of curvature smaller

than twice the reconstructed voxel size were omitted as these most likely represent noise. The non-wetting phase bulges into the wetting phase during drainage and terminal menisci thus have a positive curvature with respect to the non-wetting phase [46]. As this study is limited to drainage, all data points with a curvature equal to or smaller than zero, typically associated with arc-meniscus sections of the interface, were subsequently filtered out. Lastly, we followed the approach of [48] on the glass bead data set, to filter and weigh the curvature data points based [27,31,50] on their geodesic distance (20% of the maximum geodesic distance found in the image) to the edge of the surface. For the Ketton data set, we followed the approach of [49] by filtering data points with a Euclidian distance of 3 voxels from the pore wall.

2.3.3. Geometric (receding) contact angles

To reduce uncertainty related to the state of the interface (e.g. pinning), receding contact angles have to be measured at (or at least very near) the moment the fluid–fluid interface moves. Therefore, we propose to measure geometric contact angles at the appropriate time step in a small region directly surrounding the displacement event in time-resolved mCT data. This is in contrast to previous measurements of geometric contact angles that included all points on the three phase contact lines in a single mCT image of a static fluid distribution, typically acquired at the end of drainage or imbibition [27,31,50].

We compared both approaches of contact angle measurements using the fully automatic algorithm developed by [27]. The algorithm generated a smoothed mesh on which the three phase contact line is identified. Subsequently, it calculated geometric contact angles in each mesh point on the contact line based on the dot product of the vectors normal to the solid surface and the fluid–fluid interface. The method was applied to each time step image using the smoothing settings proposed by [27]. Event-based geometric contact angles were then determined by retaining and averaging only the geometric contact angle points measured in the event pores and their neighbors at the appropriate event time step (Fig. 2C). We compared this to the conventional static method by

calculating the distribution of all the contact angle points in the last time step of drainage.

2.3.4. Thermodynamically-consistent receding contact angles

Here, we extend the work of Morrow [40] and Blunt et al. [31] to derive a thermodynamically-consistent contact angle, θ_t , for filling events during primary drainage:

$$\cos\theta_t = \frac{2\kappa_{thr}\Delta V_{nwp} + \Delta A_{fluid-fluid}}{\Delta A_{nwp-solid}} \quad (4)$$

where κ_{thr} is the threshold mean curvature at invasion, ΔV_{nwp} the change in volume of the non-wetting phase (positive for primary drainage), $\Delta A_{fluid-fluid}$ the change in fluid–fluid interfacial area, and $\Delta A_{nwp-solid}$ the change in non-wetting–solid surface area (positive for primary drainage). Surface areas were calculated on triangulated surfaces extracted using the method described in Section 2.3.2. By applying this relationship, drainage is assumed to be an isothermal, reversible process, which has been shown not to be valid in general [35,38,40]. The calculated thermodynamically-consistent contact angle is therefore likely an underestimation, as part of the work done will be lost as viscous dissipation [31]. Similar to the calculation of the geometric receding contact angle, we compare the event-by-event based results to a static calculation using surface areas, curvatures and volumes of consecutive time step images.

3. Results & discussion

3.1. Filling events

By detecting changes in pore occupancy during the experiments and clustering these into pore filling events (Section 2), 231 (glass bead pack) and 425 (Ketton limestone) filling events were detected and analyzed (Table 2). Up to 17 (glass beads) and 8 (Ketton limestone) different events were detected in a single time step (Fig. 3). The number of pore-filling events per time step increases over time (Fig. 3) while the volumes of these events decreases (Fig. 4). Well connected, larger pores were filled first, and smaller pores with fewer connections were filled later in the sequence, as expected from invasion percolation.

3.2. Validation of curvature measurements

The force-based contact angle introduced in this paper depends crucially on the measurement of interfacial curvature from the time-resolved mCT scans. Using Eq. (1), these measurements also yield the associated capillary pressure, which can be plotted against the wetting saturation determined from the image

Table 2
Overview of the detected events in the glass bead pack and Ketton limestone.

	glass bead pack	Ketton limestone
Number of identified events	231	425
Number of multi-pore events	95	134
Number of large pore events (filling > 1% of pore volume per event.)	20	4
Number of pores in the largest event	18	46

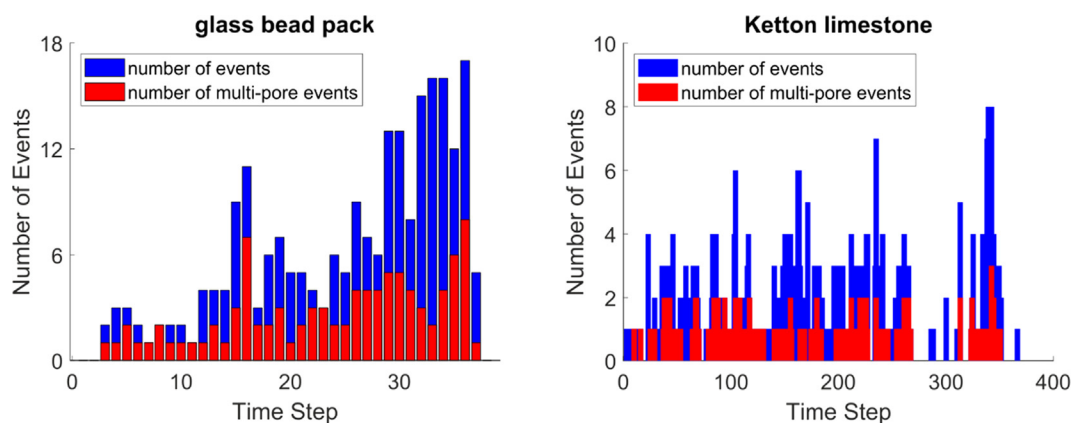


Fig. 3. Bar charts showing the number of (multi-pore) events detected per time step.

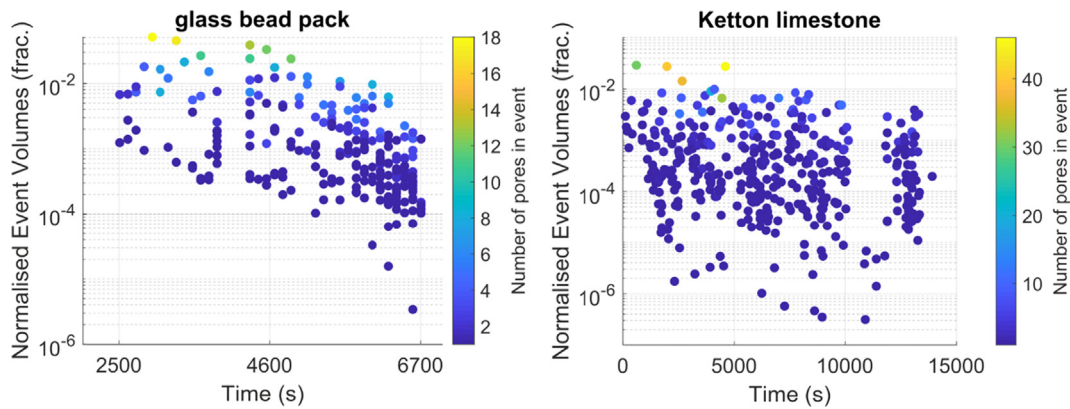


Fig. 4. Plots showing the normalized event volume for each event with the number of pores filled during the event in colors. (For interpretation of the references to colour in this figure legend, the reader is referred to the web version of this article.)

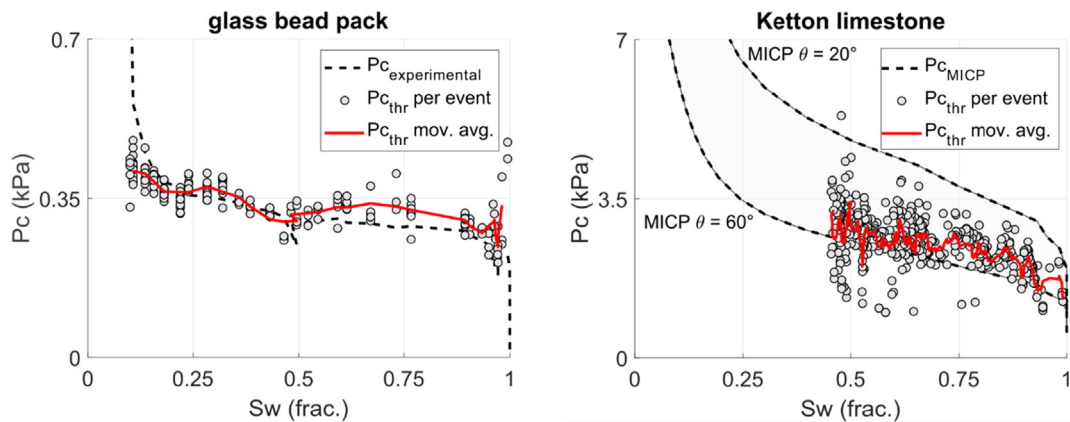


Fig. 5. Calculated threshold capillary pressure for each event plotted against the wetting-phase saturation of the sample calculated from the images. The data is compared to experimental pressure measurements in the case of the glass bead pack and scaled MICP measurements (Reynolds and Krevor 2015) using a theta between 20° and 60° for the data of the Ketton limestone.

(Fig. 5). The resulting threshold capillary pressures can thus be compared and validated to capillary pressure curves measured with external pressure transducers [46]. Experimental pressure measurements were available for the glass bead pack dataset, but not for the Ketton limestone dataset. We validated the latter using mercury intrusion capillary pressure (MICP) data, measured on a different Ketton limestone sample [51]. We rescaled the saturation axis of the MICP data to include only the pore space larger than the voxel size of the images (3.28 μm). The P_c axis was rescaled using the interfacial tension measured by [37] and a range of contact angle values (20°–60°) expected for Ketton limestone.

As can be seen in Fig. 5, the event-based calculations scatter around the externally measured pressures. The scatter is to some extent expected for drainage, since non-local effects can induce local pressure differences and the time scale of the experiments is likely too short to establish full capillary equilibrium [38,41].

Imaging and image analysis form additional sources of uncertainty. Limited spatial resolution causes uncertainty in the calculated mean curvature of the interface as the curvature is not fully resolved. Akai et al. [19] estimated that local capillary pressures can be estimated within 30% if the average radius of curvature is more than 6 times the image resolution. Applying these rules of thumb, a radius of curvature of 6 times the image resolution would be equivalent to capillary pressures of ~ 0.7 kPa and ~ 2.6 kPa for the glass beads and Ketton limestone respectively. As these values are close to the measured pressures, the spatial resolution is likely to influence the results, especially at lower wetting phase saturations.

The limited temporal resolution of the scans causes motion artefacts and decreases the signal to noise ratio, providing additional sources of uncertainty. Furthermore, this also means that the curvature is determined a few tens of seconds before the Haines jump. To estimate the uncertainty induced by this, we determined the average rate of change of the external P_c measurement in the glass bead pack. This was ~ 43 Pa per time step, equating to an uncertainty of approximately 10% on the average measured event pressures. However, the uncertainty is less significant in the beginning of drainage, and more significant at the very end (when the P_c is changing more rapidly). The temporal uncertainty on the Ketton dataset can be assumed to be lower, as both the flow rate and the time per image are smaller (Table 1), yet there are no external pressure measurements available to estimate this quantitatively. Newer synchrotron beamline setups allow to further increase the temporal resolution by 2 orders of magnitude (1 s/scan) without compromising the image quality [52,53].

3.3. Force-based, geometric and thermodynamically consistent contact angles

The distribution of the force-based contact angles is compared to those of the static and event-based geometric contact angles and of the event-based thermodynamically consistent contact angles in Fig. 6. The average force-based contact angle was 63° and 56° in respectively the glass bead pack and the Ketton limestone datasets, compared to an average event-based geometric

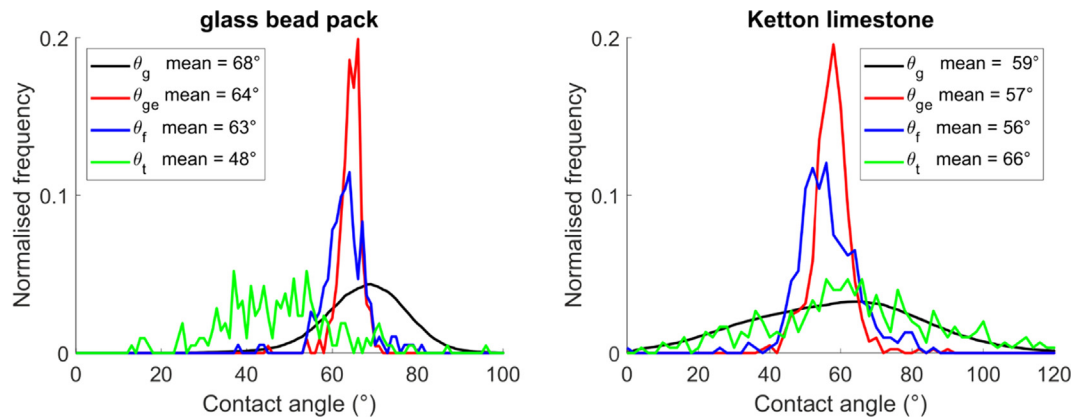


Fig. 6. Distribution of force-based (θ_f), geometric (θ_{ge}) and thermodynamically consistent (θ_t) contact angles determined on an event-by-event basis using the proposed methodology, compared to the standard approach of determining the geometric contact angles in each point on the contact line of the mCT image taken after drainage (θ_g).

contact angle of respectively 64° and 57° . The distribution of the event-based geometric contact angles matched the force-based angle closely. The event-based geometric contact angle has a notably narrower distribution than its “static” counterpart (the distribution of all geometric contact angles measured in one time step image). This confirms that the unexpectedly wide contact angle distributions reported in literature are to a significant extent related to the dynamics of the interface motion, e.g. contact angle hysteresis, pinning, the location of the contact line at the time of fluid redistribution, or interface relaxation. The event-based thermodynamically consistent contact angles are more broadly distributed than the geometric and force-based methods. They had a lower mean value than the other methods for the glass beads (48°) and a higher value for Ketton limestone (66°). Similar values, 44° and 68° for the glass bead pack and Ketton limestone respectively, were found when using the approach of [31], using the full fluid distributions on consecutive images for the calculations.

Fig. 7 shows how the determined contact angles varied over the course of the experiments. Event-based geometric and force-based contact angles remain almost constant over time for both data sets. The calculated thermodynamically consistent contact angles show considerably more spread compared to the other two methods, which was found to increase over the duration of the experiment. This is likely related to increasing errors in determining the fluid-solid surface areas as smaller pores are invaded. The average thermodynamically consistent contact angle for the glass bead pack data set is negatively correlated with time.

The contact angle values for each event are cross-plotted in Fig. 8. The fairly good match between the force-based and the geo-

metric methods suggests that geometric contact angles can be used to provide a reasonable prediction of the invasion capillary pressure in pore scale drainage models, yet only when measured on an event-by-event basis in a time-resolved dataset. This is crucial for e.g. pore network modelling studies, which predict the drainage filling sequence by sequentially invading pores in order of increasing threshold capillary pressure (invasion percolation). However, it is also clear that there was still a significant amount of scatter in the data, related to the spatial and temporal resolutions on the one hand and the irregular shape of the throats in realistic porous materials on the other hand. The latter could be improved by refining the definition of the force-based contact angle (Eq. (2)). Both sources of uncertainty are consistent with higher scatter in Ketton than in the simpler, wider pore space of the glass bead pack. The calculated thermodynamically consistent contact angles show significantly more scattering than the force-based contact angles (Fig. 8). In addition, the equation yielded imaginary values for the contact angle for 17 events in the glass bead pack data set and 125 in the Ketton limestone data set. The increased scatter could be attributed to both the added uncertainty in the calculations of fluid-fluid and fluid-solid surface areas and the assumption of no viscous dissipation.

Intuitively, receding contact angles in smooth, water-wet media are expected to be lower than the reported values. Manual observations using the method described by [54] confirmed contact angles around 50° – 60° (e.g. Fig. 2) in both the glass beads and Ketton limestone data set, showing that these were likely not induced by the automatic image analysis method. As shown in Fig. 8, the calculated values were consistent with a description of the fluid

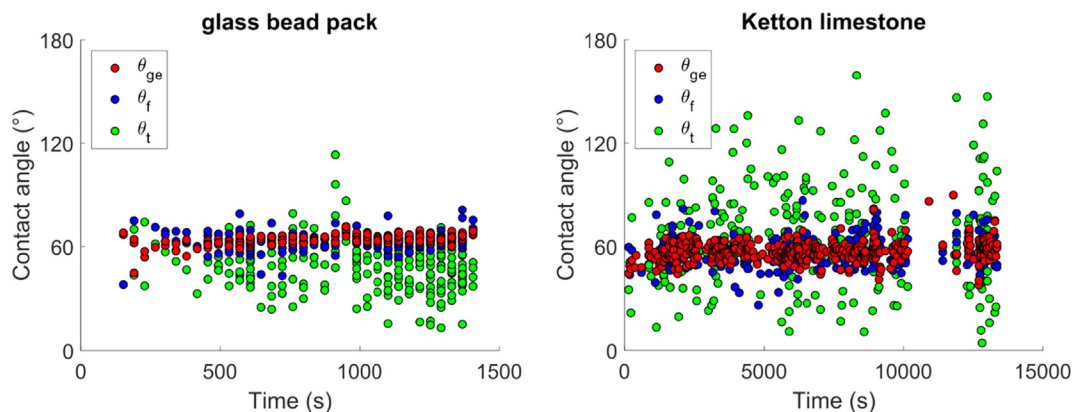


Fig. 7. Calculated force-based (θ_f), geometric (θ_{ge}) and thermodynamically consistent (θ_t) contact angles per event over the duration of the experiment.

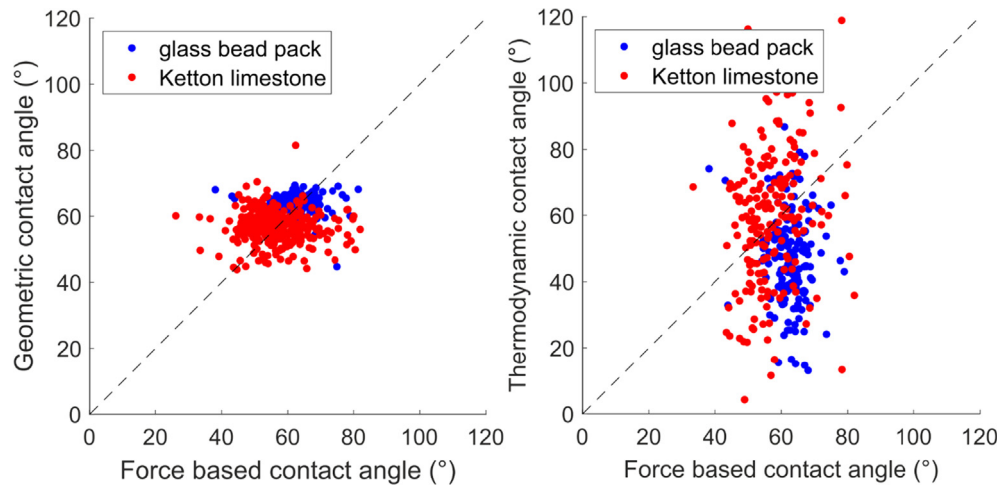


Fig. 8. Left: the geometric versus the force-based contact angle for individual events detected in the two drainage datasets. Right: the thermodynamically consistent versus the force-based contact angle for individual events in the two drainage datasets.

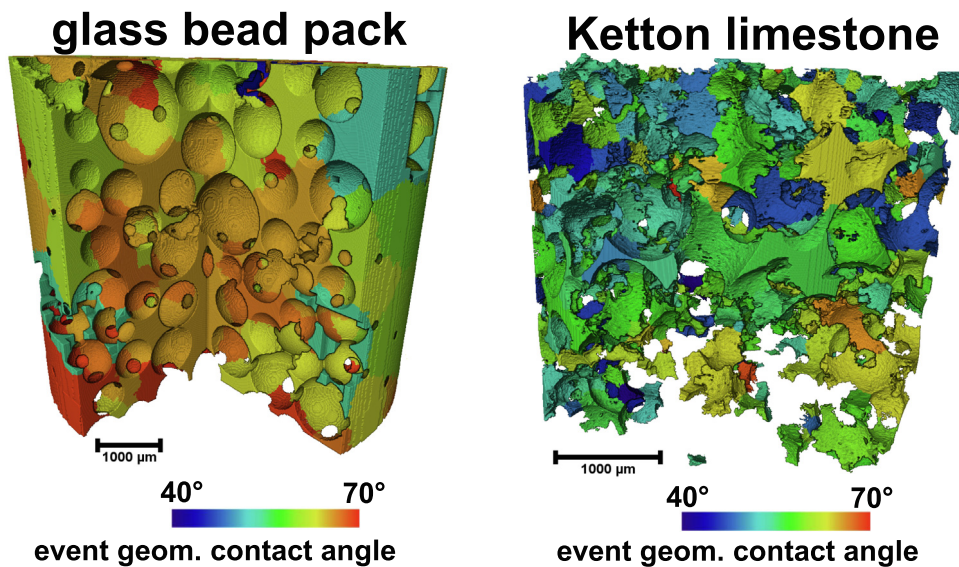


Fig. 9. Rendering of the 3D distribution of the event-based geometric contact angle for each pore.

displacement at the scale of observation, and can thus be used directly for pore scale modelling. The discrepancy may be due to the converging geometry of pore throats, which was shown to increase the “effective” contact angle (i.e. the one linked to the fluid-fluid interfacial curvature) [33]. Finally, it should also be noted that the limited temporal resolution of the mCT data tended to yield an underestimation of the fluid-fluid curvature, as the capillary pressure rises continuously during image acquisition, resulting in a slight overestimation of the contact angles.

As shown in Fig. 9, the values of event-based contact angles can be mapped back to the original pore space. This spatial data could be used to improve numerical simulations of multiphase flow by incorporating local information on the wettability of the sample, which could be especially valuable for samples with a mixed-wettability.

4. Conclusion and outlook

This work aims to improve our understanding of wettability by calculating receding contact angles for individual pore-filling

events, rather than for a static fluid distribution as a whole. The proposed method was applied to two unsteady state drainage data sets: a sintered glass bead pack and a Ketton limestone. Event-based geometric contact angles show a distinctively narrower distribution than when these are calculated on the entire static fluid distributions [27,31,50], suggesting that wide contact angle distributions are likely caused by the unaccounted for dynamics of the interface. We introduce a force-based contact angle, which shows that event-based geometric contact angles produce plausible threshold capillary pressures for associated pore filling events. This suggests that event-based geometric contact angles may provide valid effective contact angles for the displacement process and are more appropriate for use in pore scale modeling. Despite these promising first results, we note the need for enhanced image quality and image processing methodologies to reduce the uncertainty of the proposed methods. Due to these uncertainties, we were not able to draw conclusions on the appropriateness of the thermodynamic contact angle as a concept.

Future work should point out if the described method can be used to quantify wettability for mixed-wettability systems and

during imbibition. The success hereof would benefit of the increased temporal and spatial resolution available at synchrotron facilities optimized for fast imaging [52] and advances in iterative reconstruction techniques developed for low signal to noise ratios [55,56]. This enhanced image quality is crucial to distinguish different displacement mechanism during imbibition and to improve the accuracy in calculating interfacial curvature and area.

CRedit authorship contribution statement

Arjen Mascini: Conceptualization, Methodology, Software, Formal analysis, Investigation, Writing - original draft, Visualization. **Veerle Cnudde:** Conceptualization, Writing - review & editing, Supervision, Project administration, Funding acquisition. **Tom Bultreys:** Conceptualization, Methodology, Software, Formal analysis, Investigation, Writing - original draft, Writing - review & editing, Supervision, Project administration, Funding acquisition.

Declaration of Competing Interest

The authors declare that they have no known competing financial interests or personal relationships that could have appeared to influence the work reported in this paper.

Acknowledgements

Dr. Steffen Schlüter and Dr. Kamaljit Singh are thanked for making their data available and their helpful discussions. The two anonymous reviewers are thanked for their constructive feedback. This research received funding from the Research Foundation–Flanders (FWO, project G051418N). Tom Bultreys is a postdoctoral fellow of the Research Foundation–Flanders (FWO) and acknowledges its support under grant 12X0919N. The data used in this manuscript is freely available online, as cited in the main text.

Appendix A. Supplementary material

Supplementary data to this article can be found online at <https://doi.org/10.1016/j.jcis.2020.03.099>.

References

- [1] M. Bui, C.S. Adjiman, A. Bardow, E.J. Anthony, A. Boston, S. Brown, P.S. Fennell, S. Fuss, A. Galindo, L.A. Hackett, J.P. Hallett, H.J. Herzog, G. Jackson, J. Kemper, S. Krevor, G.C. Maitland, M. Matuszewski, I.S. Metcalfe, C. Petit, G. Puxty, J. Reimer, D.M. Reiner, E.S. Rubin, S.A. Scott, N. Shah, B. Smit, J.P.M. Trusler, P. Webley, J. Wilcox, N. Mac Dowell, Carbon capture and storage (CCS): the way forward, *Energy Environ. Sci.* 11 (2018) 1062–1176. <https://doi.org/10.1039/C7EE02342A>.
- [2] J.W. Mercer, R.M. Cohen, A review of immiscible fluids in the subsurface: Properties, models, characterization and remediation, *J. Contam. Hydrol.* 6 (1990) 107–163. [https://doi.org/10.1016/0169-7722\(90\)90043-G](https://doi.org/10.1016/0169-7722(90)90043-G).
- [3] R. Borup, J. Meyers, B. Pivovar, Y.S. Kim, R. Mukundan, N. Garland, D. Myers, M. Wilson, F. Garzon, D. Wood, P. Zelenay, K. More, K. Stroh, T. Zawodzinski, J. Boncella, J.E. McGrath, M. Inaba, K. Miyatake, M. Hori, K. Ota, Z. Ogumi, S. Miyata, A. Nishikata, Z. Siroma, Y. Uchimoto, K. Yasuda, K. Kimijima, N. Iwashita, Scientific aspects of polymer electrolyte fuel cell durability and degradation, *Chem. Rev.* 107 (2007) 3904–3951. <https://doi.org/10.1021/cr050182l>.
- [4] J.T. Gostick, M.W. Fowler, M.A. Ioannidis, M.D. Pritzker, Y.M. Volkovich, A. Sakars, Capillary pressure and hydrophilic porosity in gas diffusion layers for polymer electrolyte fuel cells, *J. Power Sources* 156 (2006) 375–387. <https://doi.org/10.1016/j.jpowsour.2005.05.086>.
- [5] W. Abdallah, J.S. Buckley, A. Carnegie, J. Edwards, B. Herold, E. Fordham, A. Graue, T. Habashy, N. Seleznev, C. Signer, H. Hussain, B. Montaron, M. Ziauddin, *Fundamentals of Wettability*, *Oilfield Rev.* 18 (2007).
- [6] K. Singh, M. Jung, M. Brinkmann, R. Seemann, Capillary-dominated fluid displacement in porous media, *Annu. Rev. Fluid Mech.* 51 (2019) 429–449. <https://doi.org/10.1146/annurev-fluid-010518-040342>.
- [7] M.J. Blunt, *Multiphase Flow in Permeable Media: A Pore-Scale Perspective*, Cambridge University Press, 2017. <https://books.google.be/books?id=GIKHdGAAQBAJ>.
- [8] J. Schmatz, J.L. Urai, S. Berg, H. Ott, Nanoscale imaging of pore-scale fluid–fluid–solid contacts in sandstone: imaging fluid–fluid–solid contacts, *Geophys. Res. Lett.* 42 (2015) 2189–2195. <https://doi.org/10.1002/2015GL063354>.
- [9] A.M. Alhammadi, A. AlRatrou, K. Singh, B. Bijeljic, M.J. Blunt, In situ characterization of mixed-wettability in a reservoir rock at subsurface conditions, *Sci. Rep.* 7 (2017). <https://doi.org/10.1038/s41598-017-10992-w>.
- [10] A. AlRatrou, M.J. Blunt, B. Bijeljic, Wettability in complex porous materials, the mixed-wet state, and its relationship to surface roughness, *Proc. Natl. Acad. Sci.* (2018) 201803734. <https://doi.org/10.1073/pnas.1803734115>.
- [11] J.S. Buckley, Effective wettability of minerals exposed to crude oil, *Curr. Opin. Colloid & Interface Sci.* 6 (2001) 191–196. [https://doi.org/10.1016/S1359-0294\(01\)00083-8](https://doi.org/10.1016/S1359-0294(01)00083-8).
- [12] A.B.D. Cassie, S. Baxter, Wettability of porous surfaces, *Trans. Faraday Soc.* 40 (1944) 546. <https://doi.org/10.1039/TF9444000546>.
- [13] M. Khishvand, A.H. Alizadeh, M. Piri, In-situ characterization of wettability and pore-scale displacements during two- and three-phase flow in natural porous media, *Adv. Water Resour.* 97 (2016) 279–298. <https://doi.org/10.1016/j.advwatres.2016.10.009>.
- [14] N.R. Morrow, Wettability and its effect on oil recovery, *J. Petrol. Technol.* 42 (1990) 1–476.
- [15] J. Murison, B. Semin, J.-C. Baret, S. Herminghaus, M. Schröter, M. Brinkmann, Wetting heterogeneities in porous media control flow dissipation, *Phys. Rev. Appl.* 2 (2014). <https://doi.org/10.1103/PhysRevApplied.2.034002>.
- [16] D. Quéré, Wetting and roughness, *Annu. Rev. Mater. Res.* 38 (2008) 71–99. <https://doi.org/10.1146/annurev.matsci.38.060407.132434>.
- [17] K. Singh, B. Bijeljic, M.J. Blunt, Imaging of oil layers, curvature and contact angle in a mixed-wet and a water-wet carbonate rock, *Water Resour. Res.* 52 (2016) 1716–1728. <https://doi.org/10.1002/2015WR018072>.
- [18] R.N. Wenzel, Resistance of solid surfaces to wetting by water, *Industr. Eng. Chem.* 28 (1936) 988–994. <https://doi.org/10.1021/ie50320a024>.
- [19] T. Akai, Q. Lin, A. Alhosani, B. Bijeljic, M. Blunt, Quantification of uncertainty and best practice in computing interfacial curvature from complex pore space images, *Materials* 12 (2019) 2138. <https://doi.org/10.3390/ma12132138>.
- [20] R. Verma, M. Icardi, M. Prodanović, Effect of wettability on two-phase quasi-static displacement: validation of two pore scale modeling approaches, *J. Contam. Hydrol.* 212 (2018) 115–133. <https://doi.org/10.1016/j.jconhyd.2018.01.002>.
- [21] B. Zhao, C.W. MacMinn, B.K. Primkulov, Y. Chen, A.J. Valocchi, J. Zhao, Q. Kang, K. Bruning, J.E. McClure, T. Miller, A. Fakhari, D. Bolster, T. Hiller, M. Brinkmann, L. Cueto-Felgueroso, D.A. Cogswell, R. Verma, M. Prodanović, J. Maes, S. Geiger, M. Vassvik, A. Hansen, E. Segre, R. Holtzman, Z. Yang, C. Yuan, B. Chareyre, R. Juanes, Comprehensive comparison of pore-scale models for multiphase flow in porous media, *Proc. Natl. Acad. Sci.* 116 (2019) 13799–13806. <https://doi.org/10.1073/pnas.1901619116>.
- [22] M. Andrew, H. Menke, M.J. Blunt, B. Bijeljic, The imaging of dynamic multiphase fluid flow using synchrotron-based X-ray microtomography at reservoir conditions, *Transp. Porous Media* 110 (2015) 1–24. <https://doi.org/10.1007/s11242-015-0553-2>.
- [23] S. Berg, H. Ott, S.A. Klapp, A. Schwing, R. Neiteler, N. Brussee, A. Makurat, L. Leu, F. Enzmann, J.-O. Schwarz, M. Kersten, S. Irvine, M. Stampanoni, Real-time 3D imaging of Haines jumps in porous media flow, *Proc. Natl. Acad. Sci.* 110 (2013) 3755–3759. <https://doi.org/10.1073/pnas.1221373110>.
- [24] T. Bultreys, W. De Boever, V. Cnudde, Imaging and image-based fluid transport modeling at the pore scale in geological materials: a practical introduction to the current state-of-the-art, *Earth Sci. Rev.* 155 (2016) 93–128. <https://doi.org/10.1016/j.earscirev.2016.02.001>.
- [25] D. Wildenschild, A.P. Sheppard, X-ray imaging and analysis techniques for quantifying pore-scale structure and processes in subsurface porous medium systems, *Adv. Water Resour.* 51 (2013) 217–246. <https://doi.org/10.1016/j.advwatres.2012.07.018>.
- [26] M. Khishvand, A.H. Alizadeh, I. Oraki Kohshour, M. Piri, R.S. Prasad, In situ characterization of wettability alteration and displacement mechanisms governing recovery enhancement due to low-salinity waterflooding: physics of low-salinity waterflooding, *Water Resour. Res.* 53 (2017) 4427–4443. <https://doi.org/10.1002/2016WR020191>.
- [27] A. AlRatrou, A.Q. Raeini, B. Bijeljic, M.J. Blunt, Automatic measurement of contact angle in pore-space images, *Adv. Water Resour.* 109 (2017) 158–169. <https://doi.org/10.1016/j.advwatres.2017.07.018>.
- [28] A. Scanziani, K. Singh, M.J. Blunt, A. Guadagnini, Automatic method for estimation of in situ effective contact angle from X-ray micro tomography images of two-phase flow in porous media, *J. Colloid Interface Sci.* 496 (2017) 51–59. <https://doi.org/10.1016/j.jcis.2017.02.005>.
- [29] C. Sun, J.E. McClure, P. Mostaghimi, A.L. Herring, S. Berg, R.T. Armstrong, Probing effective wetting in subsurface systems, *Geophys. Res. Lett.* 47 (2020) e2019GL086151. <https://doi.org/10.1029/2019GL086151>.
- [30] T. Akai, A.M. Alhammadi, M.J. Blunt, B. Bijeljic, Modeling oil recovery in mixed-wet rocks: pore-scale comparison between experiment and simulation, *Transp. Porous Media* 127 (2019) 393–414. <https://doi.org/10.1007/s11242-018-1198-8>.
- [31] M.J. Blunt, Q. Lin, T. Akai, B. Bijeljic, A thermodynamically consistent characterization of wettability in porous media using high-resolution imaging, *J. Colloid Interface Sci.* 552 (2019) 59–65. <https://doi.org/10.1016/j.jcis.2019.05.026>.
- [32] V. Cnudde, M.N. Boone, High-resolution X-ray computed tomography in geosciences: a review of the current technology and applications, *Earth Sci. Rev.* 123 (2013) 1–17. <https://doi.org/10.1016/j.earscirev.2013.04.003>.

- [33] H.S. Rabbani, B. Zhao, R. Juanes, N. Shokri, Pore geometry control of apparent wetting in porous media, *Sci. Rep.* 8 (2018), <https://doi.org/10.1038/s41598-018-34146-8>.
- [34] C. Sun, J.E. McClure, P. Mostaghimi, A.L. Herring, M. Shabaninejad, S. Berg, R.T. Armstrong, Linking continuum-scale state of wetting to pore-scale contact angles in porous media, *J. Colloid Interface Sci.* 561 (2020) 173–180, <https://doi.org/10.1016/j.jcis.2019.11.105>.
- [35] S. Seth, N.R. Morrow, Efficiency of the Conversion of Work of Drainage to Surface Energy for Sandstone and Carbonate, *SPE Reserv. Eval. Eng.* 10 (2007) 338–347, <https://doi.org/10.2118/102490-PA>.
- [36] S. Schlüter, S. Berg, M. Rücker, R.T. Armstrong, H.-J. Vogel, R. Hilfer, D. Wildenschild, Pore-scale displacement mechanisms as a source of hysteresis for two-phase flow in porous media, *Water Resour. Res.* 52 (2016) 2194–2205, <https://doi.org/10.1002/2015WR018254>.
- [37] K. Singh, H. Menke, M. Andrew, C. Rau, B. Bijeljic, M.J. Blunt, Time-resolved synchrotron X-ray micro-tomography datasets of drainage and imbibition in carbonate rocks, *Sci. Data* 5 (2018), <https://doi.org/10.1038/sdata.2018.265>.
- [38] R.T. Armstrong, S. Berg, Interfacial velocities and capillary pressure gradients during Haines jumps, *Phys. Rev. E* 88 (2013) 043010.
- [39] W.B. Haines, *Studies in the physical properties of soil. V. The hysteresis effect in capillary properties, and the modes of moisture distribution associated therewith*, *J. Agric. Sci.* 20 (1930) 97–116.
- [40] N.R. Morrow, Physics and thermodynamics of capillary action in porous media, *Ind. Eng. Chem.* 62 (1970) 32–56, <https://doi.org/10.1021/ie50726a006>.
- [41] S. Schlüter, S. Berg, T. Li, H.-J. Vogel, D. Wildenschild, Time scales of relaxation dynamics during transient conditions in two-phase flow: relaxation dynamics, *Water Resour. Res.* 53 (2017) 4709–4724, <https://doi.org/10.1002/2016WR019815>.
- [42] S. Ma, G. Mason, N.R. Morrow, Effect of contact angle on drainage and imbibition in regular polygonal tubes, *Colloids Surf., A: Physicochem Eng. Aspects* 117 (1996) 273–291, [https://doi.org/10.1016/0927-7757\(96\)03702-8](https://doi.org/10.1016/0927-7757(96)03702-8).
- [43] V. Joekar-Niasar, M. Prodanović, D. Wildenschild, S.M. Hassanizadeh, Network model investigation of interfacial area, capillary pressure and saturation relationships in granular porous media: new network model for capillary flow, *Water Resour. Res.* 46 (2010), <https://doi.org/10.1029/2009WR008585>.
- [44] A.Q. Raeini, B. Bijeljic, M.J. Blunt, Generalized network modeling of capillary-dominated two-phase flow, *Phys. Rev. E* 97 (2018), <https://doi.org/10.1103/PhysRevE.97.023308>.
- [45] M. Andrew, B. Bijeljic, M.J. Blunt, Pore-by-pore capillary pressure measurements using X-ray microtomography at reservoir conditions: Curvature, snap-off, and remobilization of residual CO₂, *Water Resour. Res.* 50 (2014) 8760–8774, <https://doi.org/10.1002/2014WR015970>.
- [46] R.T. Armstrong, M.L. Porter, D. Wildenschild, Linking pore-scale interfacial curvature to column-scale capillary pressure, *Adv. Water Resour.* 46 (2012) 55–62, <https://doi.org/10.1016/j.advwatres.2012.05.009>.
- [47] W.E. Lorensen, H.E. Cline, Marching cubes: A high resolution 3D surface construction algorithm, in: *ACM Siggraph Computer Graphics*, ACM, 1987: pp. 163–169.
- [48] T. Li, S. Schlüter, M.I. Dragila, D. Wildenschild, An improved method for estimating capillary pressure from 3D microtomography images and its application to the study of disconnected nonwetting phase, *Adv. Water Resour.* 114 (2018) 249–260, <https://doi.org/10.1016/j.advwatres.2018.02.012>.
- [49] K. Singh, H. Menke, M. Andrew, Q. Lin, C. Rau, M.J. Blunt, B. Bijeljic, Dynamics of snap-off and pore-filling events during two-phase fluid flow in permeable media, *Sci. Rep.* 7 (2017), <https://doi.org/10.1038/s41598-017-05204-4>.
- [50] L.E. Dalton, K.A. Klise, S. Fuchs, D. Crandall, A. Goodman, Methods to measure contact angles in scCO₂-brine-sandstone systems, *Adv. Water Resour.* 122 (2018) 278–290, <https://doi.org/10.1016/j.advwatres.2018.10.020>.
- [51] C.A. Reynolds, S. Krevor, Characterizing flow behavior for gas injection: Relative permeability of CO₂-brine and N₂-water in heterogeneous rocks: characterizing flow behavior for gas injection, *Water Resour. Res.* 51 (2015) 9464–9489, <https://doi.org/10.1002/2015WR018046>.
- [52] R. Mokso, C.M. Schlepütz, G. Theidel, H. Billich, E. Schmid, T. Celcer, G. Mikuljan, L. Sala, F. Marone, N. Schlumpf, et al., GigaFROST: the gigabit fast readout system for tomography, *J. Synchrotron Radiat.* 24 (2017) 1250–1259.
- [53] C. Spurin, S.C. Krevor, M.J. Blunt, S. Berg, B. Bijeljic, T. Bultreys, M. Rücker, G. Garfi, A. Scanziani, C.M. Schlepütz, et al., Imaging of steady-state intermittent flow pathways in a carbonate rock with 1 second time resolution, in: *AGU Fall Meeting 2019*, AGU, 2019.
- [54] M. Andrew, B. Bijeljic, M.J. Blunt, Pore-scale contact angle measurements at reservoir conditions using X-ray microtomography, *Adv. Water Resour.* 68 (2014) 24–31, <https://doi.org/10.1016/j.advwatres.2014.02.014>.
- [55] G.-H. Chen, J. Tang, S. Leng, Prior image constrained compressed sensing (PICCS): a method to accurately reconstruct dynamic CT images from highly undersampled projection data sets, *Med. Phys.* 35 (2008) 660–663.
- [56] G.R. Myers, A.M. Kingston, T.K. Varslot, M.L. Turner, A.P. Sheppard, Dynamic tomography with a priori information, *Appl. Opt.* 50 (2011) 3685–3690.